We are IntechOpen, the world's leading publisher of Open Access books Built by scientists, for scientists

4,800
Open access books available

122,000
International authors and editors

135M
Downloads

Our authors are among the

154
Countries delivered to

TOP 1%
most cited scientists

12.2%
Contributors from top 500 universities

WEB OF SCIENCE™

Selection of our books indexed in the Book Citation Index in Web of Science™ Core Collection (BKCI)

Interested in publishing with us?
Contact book.department@intechopen.com

Numbers displayed above are based on latest data collected.
For more information visit www.intechopen.com

8

A Fourth-Order Runge-Kutta Method with Low Numerical Dispersion for Simulating 3D Wave Propagation

Dinghui Yang, Xiao Ma, Shan Chen and Meixia Wang
Department of Mathematical Sciences, Tsinghua University, Beijing, China

1. Introduction

The numerical solutions of the acoustic-wave equation via finite-differences, finite-elements, and other related numerical techniques are valuable tools for the simulation of wave propagation. Many numerical methods of modeling waves propagating in various different media have been proposed in past three decades (Kosloff & Baysal, 1982; Booth & Crampin, 1983; Virieux, 1986; Dablain, 1986; Chen, 1993; Carcione, 1996; Blanch & Robertsson, 1997; Komatitsch & Vilotte, 1998; Carcione & Helle, 1999; Carcione et al., 1999; Moczo et al., 2000, Yang et al., 2002, 2006, 2007; many others). These modeling techniques for the 1D and 2D cases are typically used as support for a sound interpretation when dealing with complex geology, or as a benchmark for testing processing algorithms, or used in more or less automatic inversion procedure by perturbation of the parameters characterizing the elastic medium until the synthetic records fit the observed real data. In these methods, the finite-difference (FD) methods were leader and popularly used in Acoustics, Geophysics, and so on due to their simplicity for computer codes.

However, it is well-known that the conventional finite-difference (FD) methods for solving the acoustic wave equation often suffer from serious numerical dispersion when too few grid points per wavelength are used or when the models have large velocity contrasts, or artefacts caused by the source at grid points (Fei & Larner 1995, Yang et al., 2002). Roughly speaking, numerical dispersion is an unphysical phenomenon caused by discretizing the wave equation (Sei & Symes, 1995; Yang et al., 2002). Such a phenomenon makes the wave's velocity frequency dependent. More high-order or accurate FD operators have been developed to minimize the dispersion errors, and those modified FD schemes greatly improved the computational accuracy compared to the conventional operators. For example, the staggered-grid FD method with local operators (Virieux, 1986; Fornberg, 1990; Igel et al., 1995) is an efficient and convenient scheme which improves the local accuracy and has better stability without increasing computation cost and memory usage compared to the conventional second-order FD method. However, the staggered-grid (SG) method still suffers from the numerical dispersion when too few sampling points per minimum wavelength are used and may result in the numerical anisotropy and induce additional numerical errors (Virieux, 1986; Igel et al., 1995). Dablain (1986) developed a series of high-

order FD schemes for solving the acoustic wave equation, which greatly improved the computational accuracy. But these high-order schemes also can not cure the numerical dispersion effectively when coarse grids are used, and they usually involve in more grids in a spatial direction than low-order schemes (Yang et al., 2006). For example, the tenth-order compact FD scheme (e.g., Wang et al., 2002), which usually uses more grids than low order schemes, also suffers from numerical dispersion. The demand for more grids in high-order FD methods prevents the algorithms from efficient parallel implementation and artificial boundary treatment. The flux-corrected transport (FCT) technique was suggested for eliminating the numerical dispersion (Fei & Larner 1995, Zhang et al., 1999, Yang et al, 2002; Zheng et al., 2006), but the FCT method can hardly recover the resolution lost by numerical dispersion when the spatial sampling becomes too coarse (Yang et al., 2002). On the other hand, waves have inherent dispersions as they propagate in porous media with fluids. This implies that two kinds of dispersions (numerical dispersion and physical dispersion) might occur simultaneously in wave fields if the conventional FD methods are used to compute the wave fields in a porous medium. In such a case, it is not a good idea to use the FCT technique to eliminate the numerical dispersions because we do not know how to choose the proper control parameters used in the FCT method for suppressing the numerical dispersions (Yang et al., 2006). The pseudo-spectral method (PSM) is attractive as the space operators are exact up to the Nyquist frequency, but it requires the Fourier transform (FFT) of wave-field to be made, which is computationally expensive for 3D anisotropic models and has the difficulties of handling non-periodic boundary conditions and the non-locality on memory access of the FFT, which makes the parallel implementation of the algorithms and boundary treatments less efficient (Mizutani et al., 2000). Meanwhile, it also suffers from numerical dispersion in the time direction, and its numerical dispersion is serious as the Courant number, defined by $\alpha = c_0 \Delta t / \Delta x$ (Dablain 1986; Sei & Symes, 1995), is large, i.e. as the time increment is large (Yang et al., 2006).

Another easy way to deal with the numerical dispersion is to use fine grids to increase spatial samples per wavelength. For example, a spatial sampling rate of more than 20 points per shortest wavelength is needed when a second-order FD scheme is used to obtain reliable results (Holberg, 1987), whereas a fourth-order scheme seems to produce accurate results at ten grid points per shortest wavelength. Dablain (1986) states that eight and four grid points at the Nyquist frequency are required to eliminate numerical dispersion using second-order and fourth-order FD methods, respectively. More grid points per wavelength mean more computational cost and storage. It is not advisable to apply these techniques in large-scale computation, especially for a large scale 3D simulation of seismic wave propagation because of an intensive use of Central Processing Unit (CPU) time and the requirement of a large amount of direct-access memory. Fortunately, with the rapid development of computer performance and the birth of parallel technology in past several decades, 3D wave simulation through using different numerical methods on a large scale or high frequencies becomes affordable, and the study of 3D numerical techniques has been a hot spot and rapidly developed because of its applying to practical issues in the fields of Acoustics and Geophysics.

Recently, the so-called nearly analytic discrete (NAD) method and optimal NAD (ONAD) (Yang et al., 2006) suggested by Yang et al. (2003) for acoustic and elastic equations, which was initially developed by Konddoh et al. (1994) for solving parabolic and hyperbolic

equations, is another effective method for decreasing the numerical dispersion. The method, based on the truncated Taylor expansion and the local interpolation compensation for the truncated Taylor series, uses the wave displacement-, velocity- and their gradient fields to restructure the wave displacement-fields. On the basis of such a structure, the NAD and ONAD methods can greatly increase the computational efficiency and save the memory storage. However, the NAD method has only second-order time accuracy. The ONAD method is effective in solving the acoustic and elastic wave equations for a single-phase medium, and it can not be applied to a two-phase porous wave equations such as Biot's porous wave equations (Biot, 1956a, b), because these equations include the particle velocity $\partial U/\partial t$ (U is the wave displacement) and the ONAD method does not compute this field. More recently, the NAD and ONAD methods were also extended to solve the Biot poroelastic equations (Yang et al., 2007a) and the three-dimensional anisotropic wave equations (Yang et al., 2007b).

The main purpose of this chapter is to develop a new 3D numerical method to effectively suppress the numerical dispersion caused by the discretization of the acoustic- and elastic-wave equations through using both the local spatial difference-operator and the fourth-order Runge-Kutta (RK) method so that the numerical technique developed in this chapter has rapid computational speed and can save the memory storage. For to do this, we first transform the original wave equations into a system of first-order partial differential equations with respect to time t, then we use the local high-order interpolation of the wave displacement, the particle velocity, and their gradients to approximate the high-order spatial derivatives, which effectively converts the wave equation to a system of semi-discrete ordinary differential equations (ODEs). Finally, we use the fourth-order RK method to solve the semi-discrete ODEs, and change the 4-stage RK formula to 2-stage scheme resulting that the modified 3D RK algorithm can save the memory storage. Based on such a structure, this method has fourth-order accuracy both in time and space, and it can be directly extended to solve the two-phase porous wave equations including the particle velocity $\partial U/\partial t$ (Biot, 1956a,b) because of simultaneously obtaining the velocity fields when computing the displacement fields.

To demonstrate the numerical behavior of this new method, in this chapter we provide the theoretical study on the properties of the 3D RK method: such as stability criteria, theoretical error, numerical dispersion, and computational efficiency, and compare the numerical error of the 3D RK with those of the second-order conventional FD scheme and the fourth-order LWC method for the 3D initial value problem of acoustic wave equation. Meanwhile, we also compare the numerical solutions computed by the 3D RK with the analytical solutions, and present some wave-field modeling results of this method against those of some high-order FD schemes including the SG and LWC methods for the acoustic case. Besides, we also present the synthetic seismograms in the 3D three-layer isotropic medium and the wave field snapshots in the 3D two-layer medium and the 3D transversely isotropic medium with a vertical symmetry axis (VTI). All these promising numerical results illustrate that the 3D RK can suppress effectively the numerical dispersion caused by discretizing the wave equations when too few sampling points per minimum wavelength are used or models have large velocity contrasts between adjacent layers, further resulting in both increasing the computational efficiency and saving the memory storage when big grids are used. These numerical results also imply that simultaneously using both the wave displacement and its gradients to approximate the high-order spatial derivatives is important for both reducing the numerical dispersion and compensating the important wave field information included in the displacement and particle velocity gradients.

2. Fourth-order RK method for solving ODEs

2.1 Basic RK algorithm

Consider the following ordinary differential equation

$$\frac{du}{dt} = L(u). \tag{1}$$

Where, u is an unknown function of time t, and L is a known operator with respect to u at each spatial point (i, j, k) for the 3D case. Equation (1) can be solved as an ordinary equation using the following fourth-order Runge-Kutta method

$$\begin{cases} u^{(1)} = u^n + \dfrac{1}{2}\Delta t L(u^n), \\ u^{(2)} = u^n + \dfrac{1}{2}\Delta t L(u^{(1)}), \\ u^{(3)} = u^n + \Delta t L(u^{(2)}), \\ u^{n+1} = \dfrac{1}{3}\left(-u^n + u^{(1)} + 2u^{(2)} + u^{(3)}\right) + \dfrac{1}{6}\Delta t L(u^{(3)}). \end{cases} \tag{2}$$

Where, Δt is the temporal increment, $u^n = u(n\Delta t)$, and $u^{(1)}$, $u^{(2)}$ and $u^{(3)}$ are the intermediate variables. Equation (2) shows that the RK algorithm needs to store these three intermediate variables at each time advancing step, so the storage required for computer code is very large for 3D problems. To save storage, we can equivalently change it into the following two-stage scheme

$$\begin{cases} u^* = u^n + \dfrac{1}{2}\Delta t L(u^n) + \dfrac{1}{4}\Delta t^2 L^2(u^n), \\ u^{n+1} = \dfrac{1}{3}\left(u^n + 2u^*\right) + \dfrac{1}{3}\Delta t L(u^n) + \dfrac{1}{3}\Delta t L(u^*) + \dfrac{1}{6}\Delta t^2 L^2(u^*). \end{cases} \tag{3}$$

Where $L^2 = L \cdot L$. Algorithm (3) uses only one intermediate variable u^*, resulting in that the modified two-stage RK used in this chapter can effectively save the computer memory in the 3D wave propagation modeling.

2.2 Transformations of 3D wave equations

In a 3D anisotropic medium, the wave equations, describing the elastic wave propagation, are written as

$$\frac{\partial \sigma_{ij}}{\partial x_j} + f_i = \rho \frac{\partial^2 u_i}{\partial t^2}, \tag{4a}$$

$$\sigma_{ij} = \frac{1}{2} c_{ijkl} \left(\frac{\partial u_k}{\partial x_l} + \frac{\partial u_l}{\partial x_k}\right), \tag{4b}$$

where subscripts i, j, k and l take the values of 1, 2, 3, $\rho=\rho(x,y,z)$ is the density, u_i and f_i denote the displacement component and the force-source component in the i-th direction,

and x_1, x_2 and x_3 are x, y, and z directions, respectively. σ_{ij} are the second-order stress tensors, c_{ijkl} are the fourth-order tensors of elastic constants which satisfy the symmetrical conditions $c_{ijkl} = c_{jikl} = c_{ijlk} = c_{klij}$, and may be up to 21 independent elastic constants for a 3D anisotropic case. Specially, for the isotropic and transversely isotropic case, the 21 independent elastic constants are reduced to two Lamé constants (λ and μ) and five constants (c_{11} , c_{13} , c_{33} , c_{44} , and c_{66}) , respectively.
To demonstrate our present RK method, we transform equation (4) to the following vector equation using the stress-strain relation (4b)

$$\rho \frac{\partial^2 U}{\partial t^2} = D \cdot U + f. \tag{5}$$

Where $U = (u_1, u_2, u_3)^T$, $f = (f_1, f_2, f_3)^T$, D is a second-order partial differential operator with respect to space coordinates. For instance, for a transversely isotropic homogenous case, the partial differential operator can be written as follows

$$D = \begin{bmatrix} c_{11}\frac{\partial^2}{\partial x^2} + c_{66}\frac{\partial^2}{\partial y^2} + c_{55}\frac{\partial^2}{\partial z^2} & (c_{12}+c_{66})\frac{\partial^2}{\partial x \partial y} & (c_{13}+c_{55})\frac{\partial^2}{\partial x \partial z} \\ (c_{12}+c_{66})\frac{\partial^2}{\partial x \partial y} & c_{66}\frac{\partial^2}{\partial x^2} + c_{22}\frac{\partial^2}{\partial y^2} + c_{44}\frac{\partial^2}{\partial z^2} & (c_{23}+c_{44})\frac{\partial^2 u_z}{\partial y \partial z} \\ (c_{13}+c_{55})\frac{\partial^2}{\partial x \partial z} & (c_{23}+c_{44})\frac{\partial^2}{\partial y \partial z} & c_{55}\frac{\partial^2}{\partial x^2} + c_{44}\frac{\partial^2}{\partial y^2} + c_{33}\frac{\partial^2}{\partial z^2} \end{bmatrix}.$$

Let $w_i = \partial u_i / \partial t, i = 1,2,3$, and $W = (w_1, w_2, w_3)^T$, then equation (5) can be rewritten as

$$\begin{aligned} \frac{\partial U}{\partial t} &= W, \\ \frac{\partial W}{\partial t} &= \frac{1}{\rho} D \cdot U + \frac{1}{\rho} f. \end{aligned} \tag{6}$$

Define $V = (U, W)^T$, then equation (6) can be further written as

$$\frac{\partial V}{\partial t} = L \cdot V + F, \tag{7}$$

where $L = \begin{bmatrix} 0 & I_{3\times 3} \\ \frac{1}{\rho} D & 0 \end{bmatrix}, F = \begin{bmatrix} 0 \\ \frac{1}{\rho} f \end{bmatrix}$, $I_{3\times 3}$ is the third-order unit operator.
Define the following vectors and operator matrix:

$$\overline{V} = [V, \frac{\partial V}{\partial x}, \frac{\partial V}{\partial y}, \frac{\partial V}{\partial z}]^T ,$$

$$\bar{F} = [F, \frac{\partial F}{\partial x}, \frac{\partial F}{\partial y}, \frac{\partial F}{\partial z}]^T,$$

and

$$\bar{L} = \begin{pmatrix} L & 0 & 0 & 0 \\ 0 & L & 0 & 0 \\ 0 & 0 & L & 0 \\ 0 & 0 & 0 & L \end{pmatrix}.$$

With the previous three definitions, in a homogeneous medium, we have the following equation:

$$\frac{\partial \bar{V}}{\partial t} = \bar{L} \cdot \bar{V} + \bar{F}. \tag{8}$$

2.3 3D fourth-order RK algorithm

We suppose that equation (8) is a semi-discrete equation, on the right–hand side of which the high-order spatial derivatives are explicitly approximated by the local interpolation method (Yang et al., 2010). Under such an assumption, Equation (8) is converted to a system of semi-discrete ODEs with respect to variable $\bar{V}$, and can be solved by the fourth-order RK method (formula (3)). In other words, we can apply formula (3) to solve the semi-discrete ODEs (8) as follows

$$\bar{\mathbf{V}}^*_{i,j,k} = \bar{\mathbf{V}}^n_{i,j,k} + \frac{1}{2}\Delta t \bar{\mathbf{L}}\bar{\mathbf{V}}^n_{i,j,k} + \frac{1}{4}\Delta t^2 \bar{\mathbf{L}}^2 \bar{\mathbf{V}}^n_{i,j,k}, \tag{9a}$$

$$\bar{\mathbf{V}}^{n+1}_{i,j,k} = \frac{1}{3}\left(\bar{\mathbf{V}}^n_{i,j,k} + 2\bar{\mathbf{V}}^*_{i,j,k}\right) + \frac{1}{3}\Delta t \bar{\mathbf{L}}\bar{\mathbf{V}}^n_{i,j,k} + \frac{1}{3}\Delta t \bar{\mathbf{L}}\bar{\mathbf{V}}^*_{i,j,k} + \frac{1}{6}\Delta t^2 \bar{\mathbf{L}}^2 \bar{\mathbf{V}}^*_{i,j,k}. \tag{9b}$$

Where $\bar{V}^n_{i,j,k} = \bar{V}(n\Delta t, i\Delta x, j\Delta y, k\Delta z)$ and the differential operators can be written as

$$\begin{aligned} \bar{L} &= Diag(L, L, L, L) \\ &= Diag\left[\begin{pmatrix} 0 & I_{3\times 3} \\ \frac{1}{\rho}D & 0 \end{pmatrix}, \begin{pmatrix} 0 & I_{3\times 3} \\ \frac{1}{\rho}D & 0 \end{pmatrix}, \begin{pmatrix} 0 & I_{3\times 3} \\ \frac{1}{\rho}D & 0 \end{pmatrix}, \begin{pmatrix} 0 & I_{3\times 3} \\ \frac{1}{\rho}D & 0 \end{pmatrix}\right]. \end{aligned} \tag{10a}$$

$$\begin{aligned} \bar{L}^2 &= Diag(L^2, L^2, L^2, L^2) \\ &= Diag\left[\frac{1}{\rho}D, \ \frac{1}{\rho}D, \ \frac{1}{\rho}D, \ \frac{1}{\rho}D, \ \frac{1}{\rho}D, \ \frac{1}{\rho}D, \ \frac{1}{\rho}D, \ \frac{1}{\rho}D\right]. \end{aligned} \tag{10b}$$

From equation (9) and definitions of $\bar{L}$ and $\bar{L}^2$, we know that the calculations of $\bar{V}^*_{i,j,k}$ and $\bar{V}^{n+1}_{i,j,k}$ only involve in the second- and third-order spatial derivatives of the displacement U

and the particle velocity *W*, so we can compute these derivatives using equations (A3)-(A7) (see Appendix A).

3. Error analysis and stability conditions

In this section, we investigate the stability criteria and theoretical error of the two-stage RK scheme, and compare the numerical error of the 3D RK with those of the second-order conventional FD scheme and the fourth-order LWC method (Dablain, 1986) for the 3D initially value problem of acoustic wave equation.

3.1 Stability conditions

In order to keep numerical calculation stable, we must consider how to choose the appropriate time and the space grid sizes, Δt and h. As we know, mathematically, the Courant number defined by $\alpha = c_0 \Delta t / h$ gives the relationship among the acoustic velocity c_0 and the two grid sizes, we need to determine the range of α. Following the Fourier analysis (Richtmyer & Morton, 1967; Yang et al., 2006, 2010), after some mathematical derivations (see Appendix B for detail), we obtain the stability conditions for solving 1D, 2D, and 3D acoustic equation as follows:

$$\text{1D case: } \Delta t \le \alpha_{\max} \frac{h}{c_0} \approx 0.730 \frac{h}{c_0}, \tag{11}$$

$$\text{2D case: } \Delta t \le \alpha_{\max} \frac{h}{c_0} \approx 0.707 \frac{h}{c_0}, \tag{12}$$

$$\text{3D case: } \Delta t \le \alpha_{\max} \frac{h}{c_0} \approx 0.577 \frac{h}{c_0}. \tag{13}$$

Where, $\alpha_{\max}$ is the maximum value of the Courant number, $\Delta x = h$ for the 1D case, $\Delta x = \Delta z = h$ for the 2D case, and $\Delta x = \Delta y = \Delta z = h$ for the 3D case.

When the RK method is applied to solve the 3D elastic wave equations, we estimate that the temporal grid size should satisfy the following stability condition,

$$\Delta t \le \Delta t_{\max} \approx 0.577 \frac{h}{c_{\max}}, \tag{14}$$

where $\Delta t_{\max}$ is the maximum temporal increment that keeps the 3D RK method stable and $c_{\max}$ is the maximum *P*-wave velocity.

The stability condition for a heterogeneous medium can not be directly determined, but it could be approximated by using a local homogenization theory. Equations (11)-(14) are approximately correct for a heterogeneous medium if the maximal values of the wave velocities c_0 and $c_{\max}$ are used.

3.2 Error

To better understand the 3D RK method, we investigate its accuracy both theoretically and numerically, and we also compare it with the fourth-order LWC method (Dablain, 1986) and the second-order conventional FD method (Kelly et al., 1976).

3.2.1 Theoretical error

Using the Taylor series expansion, we find that the errors for the spatial derivatives $(\partial^{q+l+m}U / \partial x^k \partial y^l \partial z^m)^n_{i,j,k}$ $(2 \le q+l+m \le 3)$ are fourth order (i.e. $O(\Delta x^4 + \Delta y^4 + \Delta z^4)$), which results from the local interpolation as formulated in equations (A3)-(A7) in Appendix A. This conclusion is consistent with that given by Yang et al. (2007). Because the fourth-order Runge-Kutta method is used to solve the ODEs in equation (8), the temporal error, caused by the discretization of the temporal derivative, is in the order of $O(\Delta t^4)$. Therefore, we conclude that the error introduced by the two-stage RK scheme (9) is in the order of $O(\Delta t^4 + \Delta x^4 + \Delta y^4 + \Delta z^4)$. In other words, the 3D RK method suggested in this chapter has fourth-order accuracy in both time and space.

3.2.2 Numerical errors

In order to investigate the numerical error of the two-stage RK method proposed in this chapter, we consider the following 3D initial value problem:

$$\begin{cases} \dfrac{\partial^2 u}{\partial x^2} + \dfrac{\partial^2 u}{\partial y^2} + \dfrac{\partial^2 u}{\partial z^2} = \dfrac{1}{c_0^2}\dfrac{\partial^2 u}{\partial t^2}, \\ u(0,x,y,z) = \cos\left[-\dfrac{2\pi f_0}{c_0}(l_0 x + m_0 z + n_0 z) \right], \\ \dfrac{\partial}{\partial t}u(0,x,y,z) = -2\pi f_0 \sin\left[-\dfrac{2\pi f_0}{c_0}(l_0 x + m_0 z + n_0 z) \right], \end{cases} \tag{15}$$

where c_0 is the velocity of the plane wave, f_0 is the frequency, and (l_0, m_0, n_0) is the incident direction at t=0.

Obviously, the analytical solution for the initial problem (15) is given by

$$u(t,x,y,z) = \cos\left[2\pi f_0 \left(t - \frac{x}{c_0} l_0 - \frac{y}{c_0} m_0 - \frac{z}{c_0} n_0 \right) \right]. \tag{16}$$

For comparison, we also use the second-order FD method and the so-called LWC (fourth-order compact scheme (Dablain, 1986)) to solve the initial problem (15).

In the first numerical example, we choose the number of grid points N = 100, the frequency f_0=15Hz, the wave velocity c_0=2.5km/s, and $(l_0, m_0, n_0) = (\frac{1}{\sqrt{3}}, \frac{1}{\sqrt{3}}, \frac{1}{\sqrt{3}})$. The relative error ($E_r$) is the ratio of the RMS of the residual $(u^n_{j,m,l} - u(t_n, x_j, y_m, z_l))$ and the RMS of the exact solution $u(t_n, x_j, y_m, z_l)$. Its explicit definition is as follows:

$$E_r(\%) = \left\{ \frac{1}{\sum_{j=1}^{N}\sum_{m=1}^{N}\sum_{l=1}^{N}[u(t_n, x_j, y_m, z_l)]^2} \sum_{j=1}^{N}\sum_{m=1}^{N}\sum_{l=1}^{N}[u^n_{j,m,l} - u(t_n, x_j, y_m, z_l)]^2 \right\}^{\frac{1}{2}} \times 100. \tag{17}$$

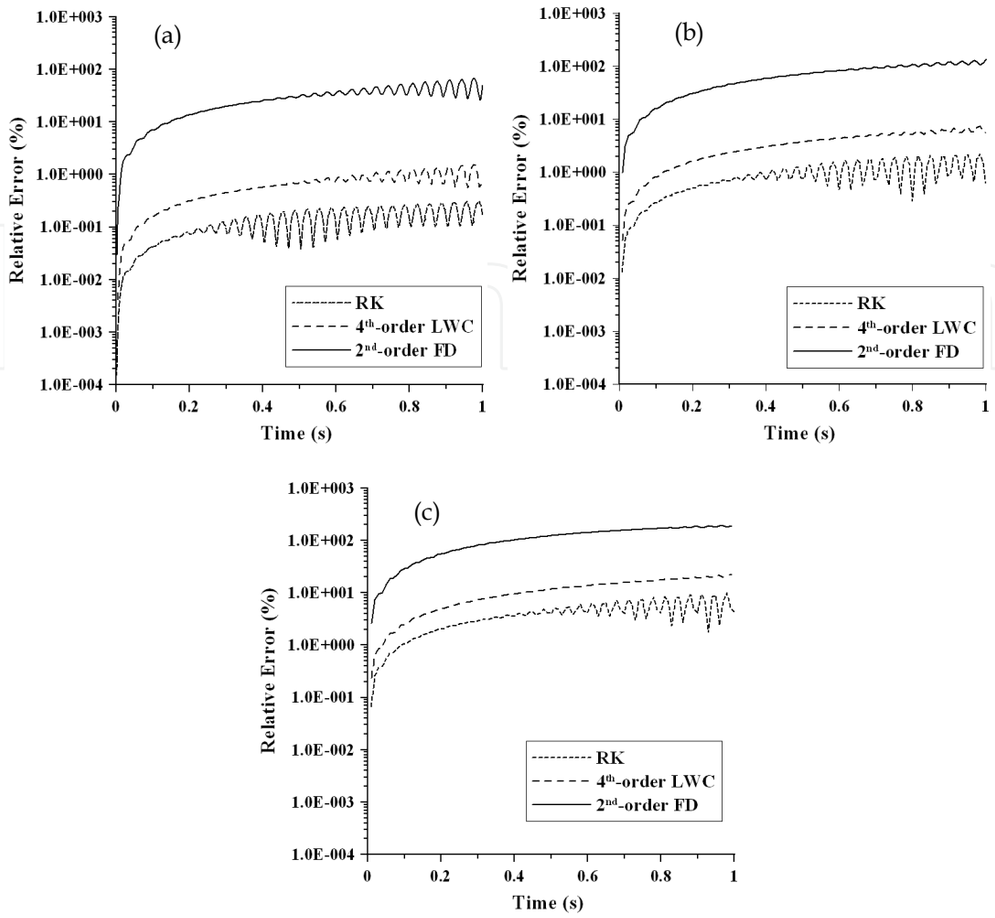

Fig. 1. The relative errors of the second-order FD, the fourth-order LWC, and the RK methods measured by E_r (formula (17)) are shown in a semilog scale for the 3D initial-value problem (15). The spatial and temporal step sizes are chosen by (a) $h=\Delta x=\Delta y=\Delta z=20$m and $\Delta t=5\times10^{-4}$s, (b) $h=\Delta x=\Delta y=\Delta z=30$m and $\Delta t=8\times10^{-4}$s, and (c) $h=\Delta x=\Delta y=\Delta z=40$m and $\Delta t=1\times10^{-3}$s, respectively.

Figures 1(a)-(c) show the computational results of the relative error E_r at different times for cases of different spatial and time increments, where three lines of E_r for the second-order FD method (line —), the fourth-order LWC (line - - - -), and the RK (line -----) are shown in a semi-log scale. In these figures, the maximum relative errors for different cases are listed in Table 1. From these error curves and Table 1 ($\Delta x=\Delta y=\Delta z=h$), we find that E_r increases corresponding to the increase in the time and/or spatial increments for all the three methods. As Figure 1 illustrated, the two-stage RK has the highest numerical accuracy among all three methods

3.3 Convergence order

In this subsection, we discuss the convergence order of the WRK method. In this case, we similarly consider the 3D initial problem (15), and choose the computational domain as $0\le x\le 1\,\text{km}$, $0\le y\le 1\,\text{km}$, $0\le z\le 1\,\text{km}$ and the propagation time T =1.0 sec. The same computational parameters are chosen as those used in subsection 3.2.2. In Table 2, we show

Method		2nd-order FD	4th-order LWC	RK
Case 1：	h=20 m $\Delta t=5\times10^{-4}$ s	1.550	2.088	0.306
Case 2：	h=30 m $\Delta t=8\times10^{-4}$ s	7.260	3.963	2.231
Case 3：	h=40 m $\Delta t=1\times10^{-3}$ s	22.298	15.715	9.949

Table 1. Comparisons of maximum relative errors of the three methods in three cases.

the numerical errors of the variable u. For the fixed spatial grid size $h=\Delta x=\Delta y=\Delta z$, the error of the numerical solution u_h with respect to the exact solution u is measured in the discrete L^1, L^2 norms

$$E_{L^m}=\left\|u_h-u\right\|_{L^m}=\left(h^3\sum_{i=1}^{N}\sum_{j=1}^{N}\sum_{k=1}^{N}\left|u_h(x_i,y_j,z_k,T)-u(x_i,y_j,z_k,T)\right|^m\right)^{\frac{1}{m}},\quad m=1,2 \tag{18}$$

h	E_{L^1}	E_{L^2}	O_{L^1}	O_{L^2}
5.000E-02	3.382E-02	5.948E-02	—	—
4.000E-02	2.073E-02	3.317E-02	2.195	2.617
2.500E-02	3.903E-03	6.190E-03	3.552	3.572
2.000E-02	1.422E-03	2.150E-03	4.524	4.738
1.000E-02	4.298E-05	6.367E-05	5.049	5.078

Table 2. Numerical errors and convergence orders of the 3D two-stage RK method.

So if we choose two different spatial steps h^{s-1} and h^s for the same computational domain, we can use (18) to get two L^k errors $E_{L^k}^{s-1}$ and $E_{L^k}^{s}$. Then the orders of numerical convergence can be defined by Dumbser et al. (2007)

$$O_{L^k}=\log\left(\frac{E_{L^k}^{s}}{E_{L^k}^{s-1}}\right)\Big/\log\left(\frac{h^s}{h^{s-1}}\right),\qquad k=1,2. \tag{19}$$

Table 2 shows the numerical errors and the convergence orders, measured by equations (18) and (19), respectively. In Table 2 the first column shows the spatial increment h, and the following four columns show L^1 and L^2 errors and their corresponding to convergence orders O_{L^1} and O_{L^2}. From Table 2 we can find that the errors E_{L^1} and E_{L^2} decrease as the spatial grid size h decreases, which implies that the 3D two-order RK method is convergent.

4. Numerical dispersion and efficiency

As we all know, the numerical dispersion or grid dispersion, which is caused by approximating the continuous wave equation by a discrete finite difference equation, is the major artifact when we use finite difference schemes to model acoustic and elastic wave-

fields, further resulting in the low computational efficiency of numerical methods. This numerical artifact causes the phase speed to become a function of spatial and time increments. The relative computational merit of most discretization schemes hinges on their ability to minimize this effect. In this section, following the analysis methods presented in Vichnevetsky (1979), Dablain (1986), and Yang et al. (2006), we investigate the dispersion relation between grid dispersion and spatial steps with the RK and the computational efficiencies for different numerical methods through numerical experiments. For comparison, we also present the dispersion results of the fourth-order SG method (Moczo et al., 2000).

4.1 Numerical dispersion

Following the dispersion analysis developed by Moczo et al. (2000) and and Yang et al. (2006), we provide a detailed numerical dispersion analysis with the RK for the 3D case in Appendix C, and compare it with the fourth-order SG method (Moczo et al., 2000). To check the effect of wave-propagation direction on the numerical dispersion, we have chosen different azimuths for two Courant numbers of $\alpha = 0.1$ and 0.3.

Figure 2 shows the dispersion relations as a function of the sampling rate S_p defined by $S_p=h/\lambda$ (Moczo et al., 2000) with h being the grid spacing and λ the wavelength. The curves correspond to different propagation directions. The results plotted in Figure 2(a) and 2(b) are computed by the dispersion relation (C4) given in Appendix C with Courant numbers of 0.1 and 0.3, respectively. Figures 2 and 3 show that the maximum phase velocity error does not exceed 11%, even if there are only 2 grid points per minimum wavelength (S_p=0.5). For a sampling rate of S_p=0.2 the numerical velocity is very close to the actual phase velocity. These Figures also shows that the dispersion curves differ for different propagation directions.

Figure 3 shows the numerical dispersion curves computed by 3D fourth-order SG using the numerical relation (C5) given in Appendix C under the same condition. In contrast with the curves in Figure 2 computed by the RK, the numerical dispersion as derived by the fourth-order SG clearly changes for different propagation directions. It is very clear that the

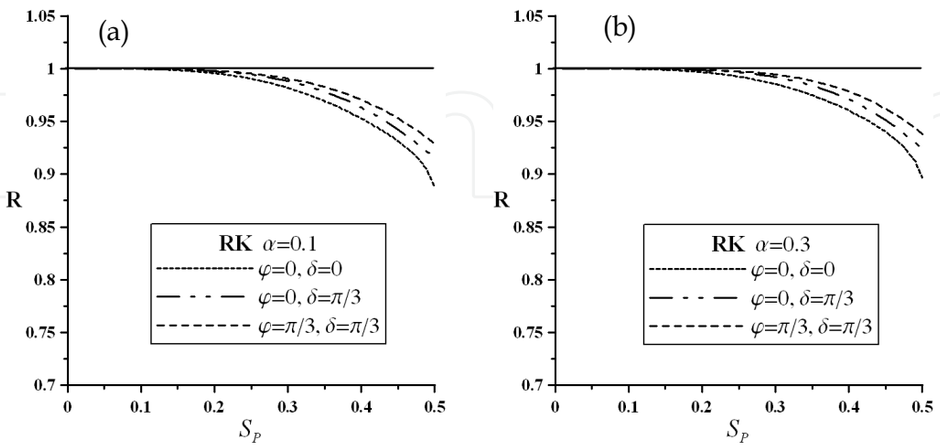

Fig. 2. The dispersion relation of RK method for the Courant number (a) $\alpha = 0.1$ and (b) $\alpha = 0.3$, in which φ is the wave propagating angle to the z-axis, and δ is the propagating angle of the wave projection in the xy plane to the x-axis.

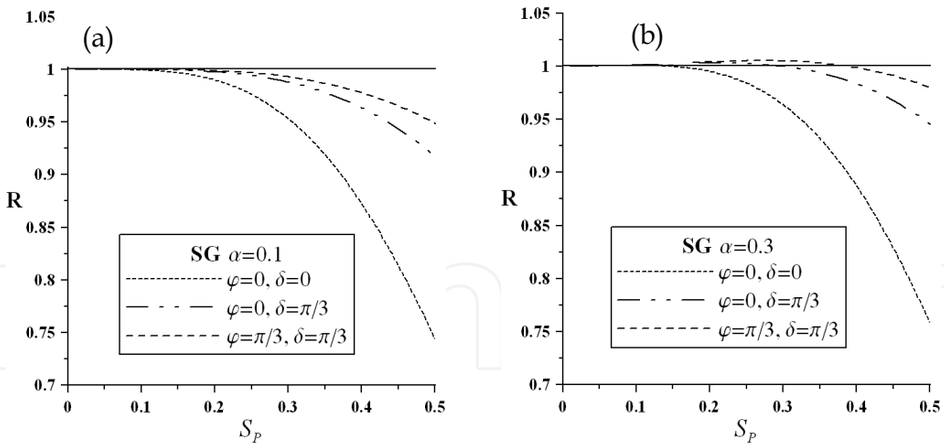

Fig. 3. The dispersion relation of the fourth-order SG method (Moczo et al., 2000) for the Courant number (a) $\alpha = 0.1$ and (b) $\alpha = 0.3$, in which φ is the wave propagating angle to the z-axis, and δ is the propagating angle of the wave projection in the xy plane to the x-axis.

numerical dispersion computed by the fourth-order SG is more serious compared with that of RK. For example, the maximum dispersion error calculated with the latter method is less than 11% (Figure 2a), while the same error calculated with the former one is greater than 26% (Figure 3a). To limit the dispersion error of the phase velocity under 8% (the maximum dispersion error by RK shown in Figure 2a), about 3 grid points per minimum wavelength are required when using fourth-order SG, opposite to only 2.1 grid points per wavelength with RK. Meanwhile, from Figure 2(a) we can observe that the numerical dispersion curves of the RK in different propagation directions are close to each other. It means that the RK has small numerical dispersion anisotropy. In contrast, from Figure 3(a) and 3(b) we can see that the difference of numerical dispersion curves in different propagation directions is very large, implying that the SG has larger numerical dispersion anisotropy than that of the RK.

After comparing Figure 2 computed by the RK with Figure 3 computed by the SG, we conclude that the RK offers smaller numerical dispersion than the SG for the same spatial sampling increment. We will verify this conclusion later via new experiments.

4.2 Computational efficiency

In this subsection, we further investigate the numerical dispersion and computational efficiency of the RK through wave-field modeling, and compare our method with the fourth-order LWC (Dablain, 1986) and the fourth-order SG method. Under this case of our consideration, we choose the following 3D acoustic wave equation

$$\frac{\partial^2 u}{\partial t^2} = c_0^2\left(\frac{\partial^2 u}{\partial x^2} + \frac{\partial^2 u}{\partial y^2} + \frac{\partial^2 u}{\partial z^2}\right) + f\,, \tag{20}$$

where c_0 is the acoustic velocity. In our present numerical experiment, we choose c_0=4 km/s. The computational domain is $0 \le x \le 5$ km, $0 \le y \le 5$ km, and $0 \le z \le 5$ km, and the number of grid points is 200×200×200. The source is a Ricker wavelet with a peak frequency of f_0 = 37 Hz. The time variation of the source function is

$$f(t) = -5.76 f_0^2 \left[1 - 16(0.6 f_0 - 1)^2\right] \exp\left[-8(0.6 f_0 - 1)^2\right] \tag{21}$$

The force-source included in equation (20) is located at the centre point of the computational domain, and *∂f/∂x* and *∂f/∂z* are set to be zero in this example and other experiments in the following section. The spatial and temporal increments are chosen by $h=\Delta x=\Delta y=\Delta z=25$ m and $\Delta t=1.5\times10^{-3}$s, respectively. The coarse spatial increment of $h=25$ m is chosen so that we test the effects of sampling rate on the numerical dispersion. A receiver R is placed at the grid point (x_R, y_R, z_R)=(3.575 km, 2.5 km, 2.5 km) to record the waveforms generated by three methods.

Following Dablain's definition (Dablain, 1986), we take the Nyquist frequency of the source to be twice the dominant frequency in this study. The rule of thumb in numerical methods for choosing an appropriate spatial step based on the Nyquist frequency can be written as

$$\Delta x = \frac{v_{\min}}{f_N \cdot G}, \tag{22}$$

where $v_{\min}$ denotes the minimum wave-velocity, f_N is the Nyquist frequency, and G denotes the number of gridpoints needed to cover the Nyquist frequency for non-dispersive propagation (Dablain, 1986). In this case chosen that implies a Nyquist frequency of 74 Hz and the number of gridpoints at Nyquist is about 2.2 in our present numerical experiment.

Figures 4, 5, and 6 show the wave-field snapshots at $t=0.5$ sec on a coarse grid of $\Delta x=\Delta y=\Delta z=25$ m ($G\approx2.2$), generated by the RK (Fig. 6), the fourth-order LWC (Dablain, 1986) (Fig. 7), and the fourth-order SG (Moczo et al., 2000) (Fig. 8), where Figures (a), (b), and (c) shown in these Figures show the wave-field snapshots in the *xy*, *xz*, and *yz* planes, respectively. Figures 7 and 8 show the wave-field snapshots at $t=0.5$ sec for the same Courant number ($\alpha = 0.24$), generated by the fourth-order LWC (Fig. 7) and the fourth-order SG (Fig. 8) on a fine grid ($\Delta x=\Delta y=\Delta z=8.3$ m) so that the numerical dispersions caused by the fourth-order LWC and the fourth-order SG are eliminated. We can see that the wavefronts of seismic waves shown in Figures 4-6, simulated by the three methods, are nearly identical. However, the result generated by the RK (Fig. 4) shows much less numerical dispersion even though the space increment is very large, whereas the fourth-order LWC and the fourth-order SG suffer from serious numerical dispersions (see Figs. 7, 8). Comparison between Figure 6 and Figures 7 and 8 demonstrates that the RK on a coarse grid can provide the similar accuracy as those of the

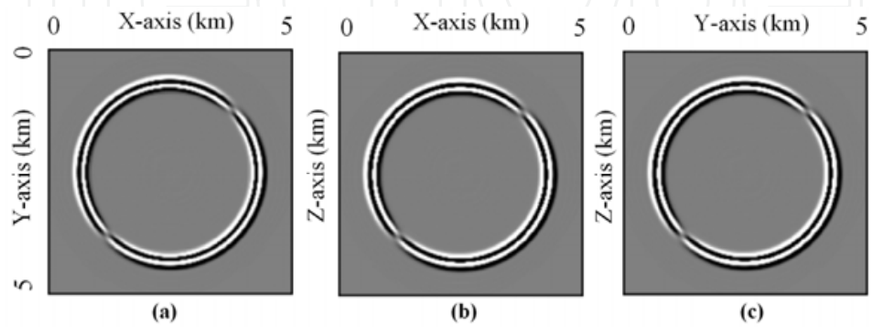

Fig. 4. Snapshots of acoustic wave fields at time 0.5 sec on the coarse grid ($\Delta x=\Delta y=\Delta z=25$m) in the *xy* (a), *xz* (b), and *yz* (c) planes, respectively, computed by the 3D RK method.

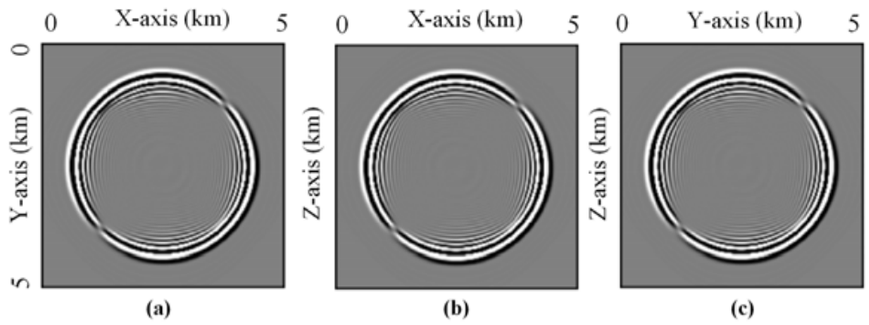

Fig. 5. Snapshots of acoustic wave fields at time 0.5 sec on the coarse grid (Δx=Δy=Δz=25 m) in the *xy* (a), *xz* (b) and *yz* (c) planes, respectively, generated by the fourth-order LWC method.

fourth-order LWC and the fourth-order SG on a fine grid for the same Courant number. But the computational cost of the RK is quite different from the other two methods. For example, it took the RK about 15.3 min to generate Figure 4, whereas the fourth-order LWC and the fourth-order SG took about 50.8 min and 50.6 min to generate Figure 5 and Figure 6, respectively. This suggests that the computational speed of the RK is roughly 3.3 times of the fourth-order LWC and the fourth-order SG to achieve the same accuracy. Thus we can conclude the 3D RK can save the computational cost by using coarse grids to simulate wave propagation in large scale models. The results in Figures 4-8 were computed on a parallel computation with 40 processors and using the message passing interface (MPI).

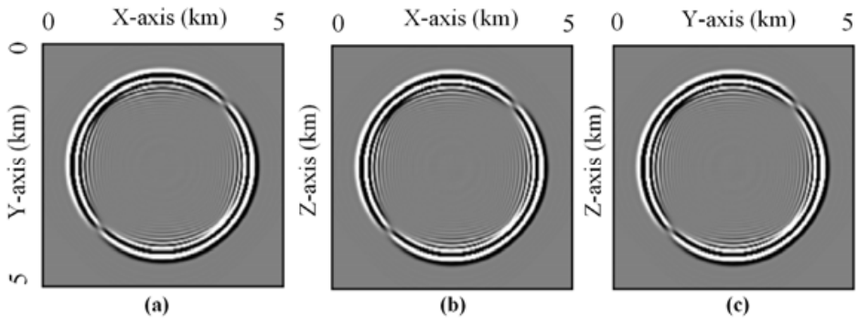

Fig. 6. Snapshots of acoustic wave fields at time 0.5 sec on the coarse grid (Δx=Δy=Δz=25 m) in the *xy* (a), *xz* (b) and *yz* (c) planes, respectively, generated by the fourth-order SG method.

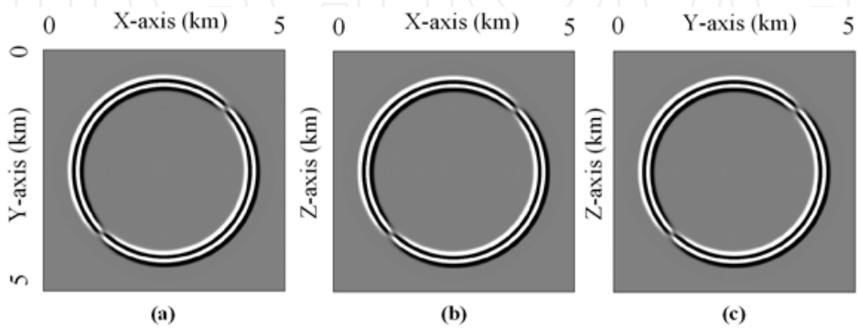

Fig. 7. Snapshots of acoustic wave fields at time 0.5 sec on the fine grid (Δx=Δy=Δz=8.3 m) in the *xy* (a), *xz* (b) and *yz* (c) planes, respectively, generated by the fourth-order LWC method.

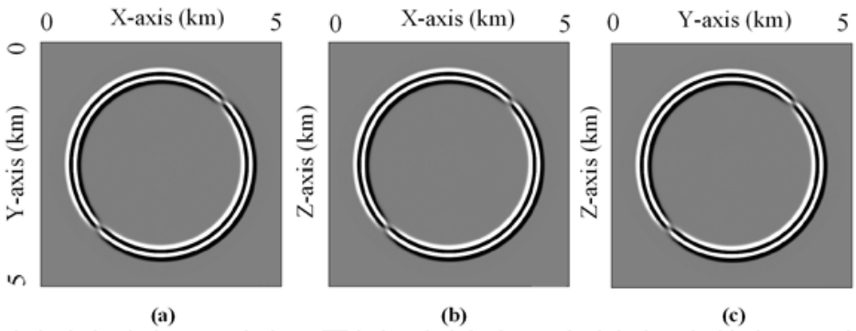

Fig. 8. Snapshots of acoustic wave fields at time 0.5 sec on the fine grid (Δx=Δy=Δz=8.3 m) in the xy (a), xz (b) and yz (c) planes, respectively, generated by the fourth-order SG method.

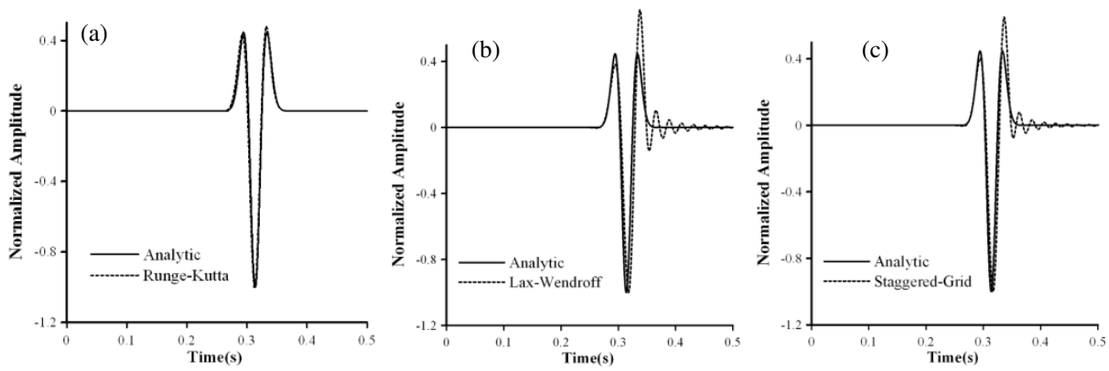

Fig. 9. Comparions of the analytic solution computed by the Cagniard–de Hoop method (de Hoop, 1960) with waveforms generated by (a) the RK, (b) the fourth-order LWC, and (c) the fourth-order SG, respectively.

Note that the memory required by RK is also different from those of the fourth-order LWC and the fourth-order SG methods. The RK needs 20 arrays to hold the wave fields at each time step, and the number of grid points for each array is 200×200×200 on a coarse grid for generating Figure 4. Even though the fourth-order LWC needs only eight arrays to store the wave displacement and the fourth-order SG needs nine arrays to store the wave displacement and the stress at each grid point to generate a comparable result, the two methods require much finer grid sampling. For example, the number of grid points of each array for generating Figures 7 and 8 goes up to 600×600×600 for both the fourth-order LWC and the fourth-order SG. Therefore, the overall memory required by the RK takes only about 31.3% of that needed by the fourth-order LWC and about 27.8% of that of the fourth-order SG.

Now we compare the accuracy of the waveforms at receiver R (3.575 km, 2.5 km, 2.5 km), generated by the RK, the fourth-order LWC, and the fourth-order SG, respectively. Figure 9 shows the waveforms of the analytic solution (solid lines) computed by the Cagniard–de Hoop method (Aki and Richards, 1980) and the numerical solutions (dashed line) computed by three numerical methods on the coarse grid (Δx=Δy=Δz=25 m). Figure 9(a) shows that the waveforms calculated by the 3D RK and the Cagniard-de Hoop method (solid line) are in good overall agreement even on the coarse grid (Δx=Δy=Δz=25 m). In contrast, the results in Figures 9(b) and 9(c), calculated by the fourth-order LWC and the SG methods,

respectively, show serious numerical dispersion following the peak wave as contrasted to the analytic solution (solid line). It illustrates that the 3D two-stage RK is accurate in wavefield modeling for the acoustic propagation modeling and it can provide very accurate results even when coarse grids are chosen.

5. Wavefield modelling

In this section, we present the performance of the two-stage RK in the 3D acoustic and elastic cases and compare against the so-called LWC method (Dablain 1986) through wavefield modelling and synthetic seismograms. In particular, we use the RK to simulate the acoustic and elastic waves propagating in the 3D multilayer acoustic medium, two-layer elastic medium, and the transversely isotropic medium with a vertical symmetry axis (VTI).

5.1 Multilayer acoustic model

In this experiment, we consider a special multilayer isotropic medium model, shown in Figure 10. Speaking in detail, when $0 \le y \le 1.5$ km, the model is consisted of three layer media where the acoustic velocities are chosen by 2 km/s, 3 km/s, and 4 km/s, corresponding to the top, middle and bottom layers, respectively, whereas the model is a two layer media with acoustic velocities of 2 km/s and 3 km/s as $1.5 \text{ km} < y \le 3$ km. The computational domain is $0 \le x \le 3$ km, $0 \le y \le 3$ km, $0 \le z \le 1.8$ km. We choose the spatial increments $\Delta x = \Delta y = \Delta z = 15$ m, the temporal increment $\Delta t = 0.8$ ms. The source of the Ricker wavelet with a peak frequency of $f_0 = 30$ Hz is located at coordinate $(x_s, y_s, z_s) = (1.5 \text{ km}, 1.5 \text{ km}, 0.015 \text{ km})$, and the expression is the same as equation (21). The perfectly matched layer (PML) absorbing boundary condition suggested by Dimitri and Jeroen (2003) is used in the experiment.

Figure 11, generated by the RK, shows the synthetic seismograms recorded by 201 receivers on the surface spreading respectively along the two lines of $y = 1.5$ km (Fig. 11a) and $x = 1.5$ km (Fig. 11b) shown in Figure 10. In Figure 11, the reflected waves from the inner interfaces are very clear. We can identify the medium structure from the reflected curve wave shown in Figure 11. In this experiment, we use the stiff boundary condition at the free surface because the source is located at the surface. This experiment also illustrates that it is efficient for the RK to combine with the PML absorbing boundary condition (Dimitri and Jeroen, 2003).

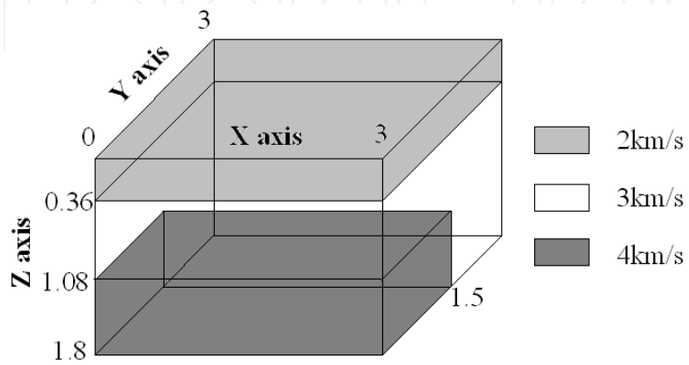

Fig. 10. The geometry of the multilayer model, which is consisted of three layer media in the domain of $0 \le y \le 1.5$ km, whereas the model is a two layer media as $1.5 \text{ km} < y \le 3$ km.

Figure 12 shows the synthetic VSP seismograms recorded in the wells, generated by the RK. In Figure 14(a), the receivers are spread from receiver R_1 (x, y, z)= (1.8 km, 1.8 km, 0) to receiver R_N (x, y, z)= (1.8 km, 1.8 km, 1.8 km) spaced 0.015 km apart, and from receiver R_1 (x, y, z)= (1.2 km, 1.2 km, 0) to receiver R_N (x, y, z)= (1.2 km, 1.2 km, 1.8 km) in Figure 12(b). From Figure 12 we can see that the VSP seismograms are very clean and have no grid dispersions while the model velocity contrasts between adjacent layers (layers 1 and 2, layers 2 and 3) are about 50% and 33%, respectively. We can also observe the difference of two seismic records shown in Figure 12(a) and 12(b) from different wells.

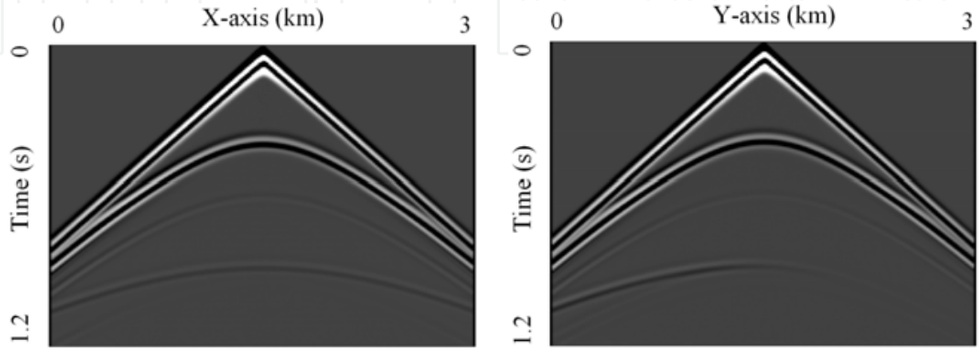

Fig. 11. Synthetic seismograms recorded by 201 receivers on the surface spreading (a) from x=0 to 3 km spaced 0.015 km apart along the line of y=1.5 km, and (b) from y=0 to 3 km spaced 0.015 km apart along the line of x=1.5 km, respectively generated by the RK for the multilayer geological model shown in Figure 14.

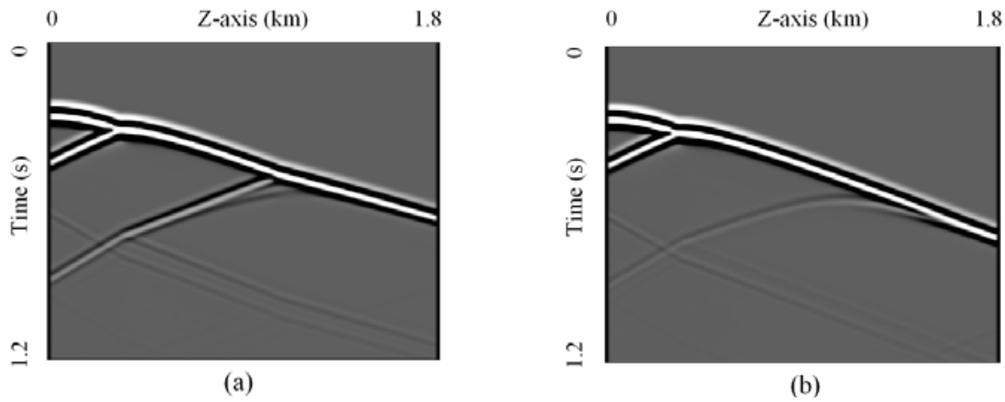

Fig. 12. Synthetic VSP seismograms recorded by 121 receivers in wells spreading (a) from receiver R_1 (x, y, z)= (1.8 km, 1.8 km, 0) to receiver R_N (x, y, z)= (1.8 km, 1.8 km, 1.8 km) , and (b) from receiver R_1 (x, y, z) =(1.2 km, 1.2 km, 0) to receiver R_N (x, y, z) =(1.2 km, 1.2 km, 1.8 km).

5.2 Two-layered elastic wave modeling

Subsurface structures have interfaces where velocities and density are discontinuous, and some of the interfaces may have strong velocity contrasts. Some FD methods, such as

conventional FD (Kelly et al., 1976), LWC method (Dablain 1986), often suffer from serious numerical dispersion when the models have large velocity contrast between adjacent layers. So we consider a two-layer medium with inner interface to investigate the validity of the 3D RK in multilayer elastic model. In the two-layer model, the Lamé constants are given as λ_1=1.5 GPa, μ_1=2.5 GPa and ρ_1=1.5g/cm^3, λ_2=11.0 GPa, μ_2=15.0 GPa and ρ_2=2.0g/cm^3, corresponding to the P- and S-wave velocities of 2.082 km/s and 1.291 km/s in the top layer medium, and 4.528 km/s and 2.739 km/s in the bottom medium. The computational domain is $0 \le x \le 4$ km, $0 \le y \le 4$ km, and $0 \le z \le 4$ km. We choose the spatial increments h=Δx=Δy=Δz=20 m and the temporal increment Δt=1.5 ms. The source of the Ricker wavelet with a peak frequency of $f_0 = 20$ Hz is located at $(x_s, y_s, z_s) = (2 \text{ km}, 2 \text{ km}, 1.92 \text{ km})$, and the source function is the same as equation (21). The three force-source components, corresponding to f_1, f_2, and f_3 included in equation (4a), are chosen by f_1=f_2=f_3=$f(t)$. The horizontal inner interface is located at the depth z=2.4 km. In this experiment, we use similarly the PML absorbing boundary condition presented in Dimitri and Jeroen (2003).

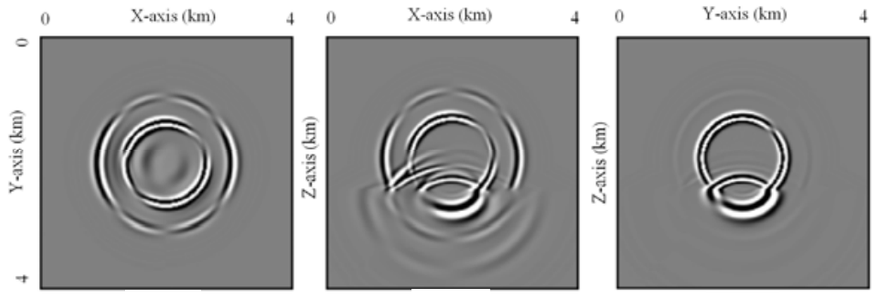

Fig. 13. Snapshots of the seismic wave fields at time 0.6 sec for the u_1 component in the two-layer isotropic medium, generated by the RK, for (a) the xy plane, (b) the xz plane, and (c) the yz plane.

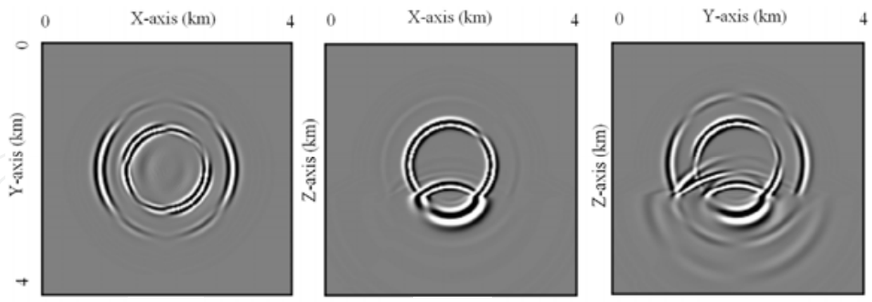

Fig. 14. Snapshots of the seismic wave fields at time 0.6 sec for the u_2 component in the two-layer isotropic medium, generated by the RK, for (a) the xy plane, (b) the xz plane, and (c) the yz plane.

Figures 13-15 show the wavefield snapshots of the three displacement-components (u_1, u_2, and u_3) at t =0.6 sec on the coarse increments (Δx=Δy=Δz=20 m) for the two-layer elastic model, generated by the RK. Figures 16-17 and Figures 18-19 show the wavefield snapshots of the horizontal and vertical displacement-components (u_1 and u_3) at t =0.6 sec for the same grid

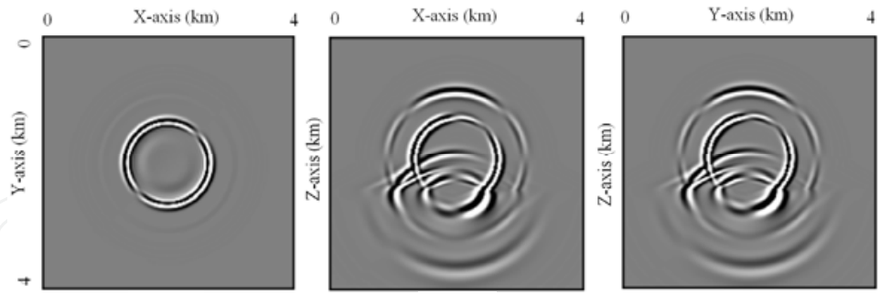

Fig. 15. Snapshots of the seismic wave fields at time 0.6 sec for the u_3 component in the two-layer isotropic medium, generated by the RK, for (a) the *xy* plane, (b) the *xz* plane, and (c) the *yz* plane.

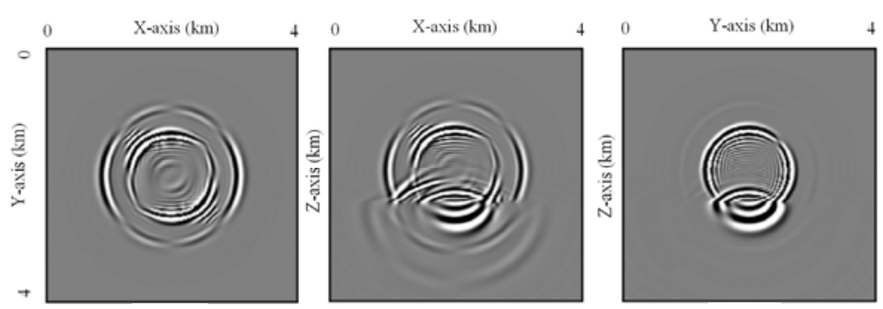

Fig. 16. Snapshots of the seismic wave fields at time 0.6 sec for the u_1 component in the two-layer isotropic medium, generated by the fourth-order LWC, for (a) the *xy* plane, (b) the *xz* plane, and (c) the *yz* plane.

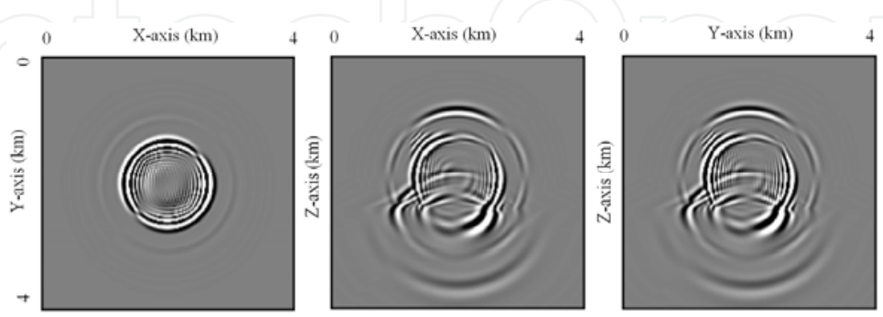

Fig. 17. Snapshots of the seismic wave fields at time 0.6 sec for the u_3 component in the two-layer isotropic medium, generated by the fourth-order LWC, for (a) the *xy* plane, (b) the *xz* plane, and (c) the *yz* plane.

increments and same model, generated by the fourth-order LWC and fourth-order SG methods, respectively. Four snapshots such as Figure 13(b) in the xz plane for the u_1 component Figure 14(c) in the yz plane for the u_2 component, and Figures 15(b) and 15(c) in the xz and yz planes for the u_3 component show numerous phases such as direct P wave, direct S wave, and their reflected, transmitted and converted phases from the inner interface. In Figures 13(c), 14(b), and 15(a), the snapshots in the yz, xz, and xy planes, corresponding to three displacement-components u_1, u_2, and u_3, respectively, show a very weak P wave and a strong S wave. The wavefield snapshots (Figs. 13-15) also show that the RK has no visible numerical dispersions even if the space increment is chosen 20 m without any additional treatments for the two-layer elastic model with a large velocity contrasts of 2.18 times between the top and bottom layer media, whereas the fourth-order LWC and the fourth-order SG suffer from substantial numerical dispersion for the same computational conditions (see Figs. 16-19).

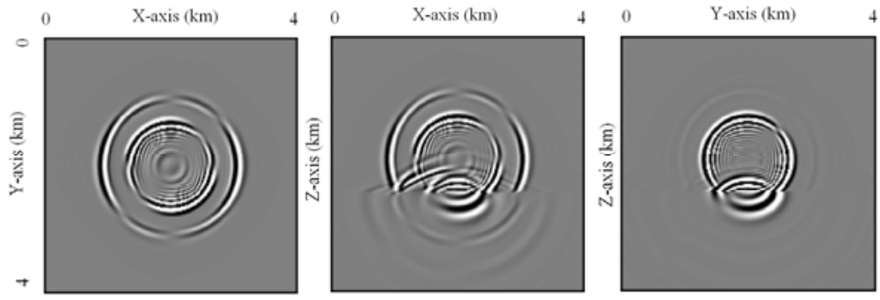

(a) (b) (c)

Fig. 18. Snapshots of the seismic wave fields at time 0.6 sec for the u_1 component in the two-layer isotropic medium, generated by the fourth-order SG, for (a) the xy plane, (b) the xz plane, and (c) the yz plane.

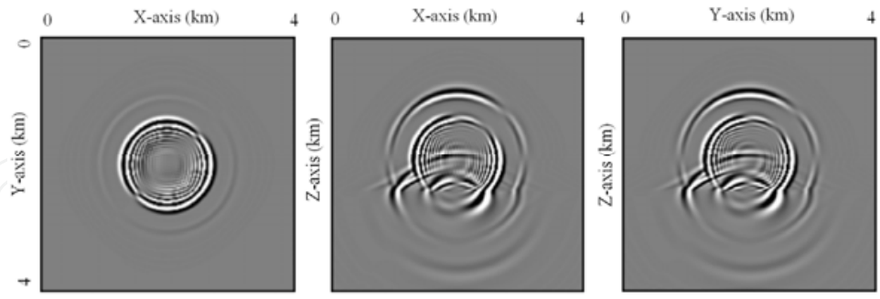

(a) (b) (c)

Fig. 19. Snapshots of the seismic wave fields at time 0.6 sec for the u_3 component in the two-layer isotropic medium, generated by the fourth-order SG, for (a) the xy plane, (b) the xz plane, and (c) the yz plane.

5.3 VTI model

In order to investigate the performance of the RK method for the anisotropic case, we simulate the elastic wave propagating in a 3D VTI medium. For this case we consider the following wave equation:

$$\begin{cases} \rho\dfrac{\partial^2 u_1}{\partial t^2} = c_{11}\dfrac{\partial^2 u_1}{\partial x^2} + c_{66}\dfrac{\partial^2 u_1}{\partial y^2} + c_{55}\dfrac{\partial^2 u_1}{\partial z^2} + (c_{12}+c_{66})\dfrac{\partial^2 u_2}{\partial x\partial y} + (c_{13}+c_{55})\dfrac{\partial^2 u_3}{\partial x\partial z} + f_1 \\ \rho\dfrac{\partial^2 u_2}{\partial t^2} = c_{66}\dfrac{\partial^2 u_2}{\partial x^2} + c_{22}\dfrac{\partial^2 u_2}{\partial y^2} + c_{44}\dfrac{\partial^2 u_2}{\partial z^2} + (c_{12}+c_{66})\dfrac{\partial^2 u_1}{\partial x\partial y} + (c_{23}+c_{44})\dfrac{\partial^2 u_3}{\partial y\partial z} + f_2 \\ \rho\dfrac{\partial^2 u_3}{\partial t^2} = c_{55}\dfrac{\partial^2 u_3}{\partial x^2} + c_{44}\dfrac{\partial^2 u_3}{\partial y^2} + c_{33}\dfrac{\partial^2 u_3}{\partial z^2} + (c_{13}+c_{55})\dfrac{\partial^2 u_1}{\partial x\partial z} + (c_{23}+c_{44})\dfrac{\partial^2 u_2}{\partial y\partial z} + f_3 \end{cases} \quad (23)$$

In this experiment, the computational domain is $0 \le x \le 5$ km, $0 \le y \le 5$ km, and $0 \le z \le 5$ km. The elastic constants and the medium density included in equation (23) are c_{11}=26.4 GPa, c_{33}=15.6 GPa, c_{13}=6.11 GPa, c_{44}=4.38 GPa, c_{66}=6.84 GPa, $c_{22} = c_{11}$, $c_{23} = c_{13}$, $c_{55} = c_{44}$, $c_{12} = c_{11} - 2c_{66}$, and ρ=2.17 g/cm^3, respectively. The source with the peak frequency f_0=17 Hz is located at the center of the computational domain as defined in equation (21). The spatial and temporal increments are $\Delta x = \Delta y = \Delta z = 25$ m and $\Delta t = 1.0 \times 10^{-3}$ sec, respectively, resulting in 3.3 grid points per minimum wavelength because the minimal qS wave velocity is 1.4207 km/sec from the elastic constants and the medium density.

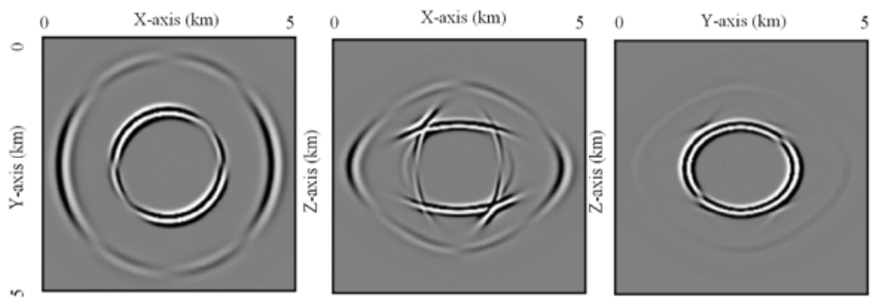

(a) (b) (c)

Fig. 20. Snapshots of elastic wave fields at time 0.7 sec for the x direction displacement (u_1) in the VTI medium, generated by the RK for (a) the xy plane, (b) the xz plane, and (c) the yz plane.

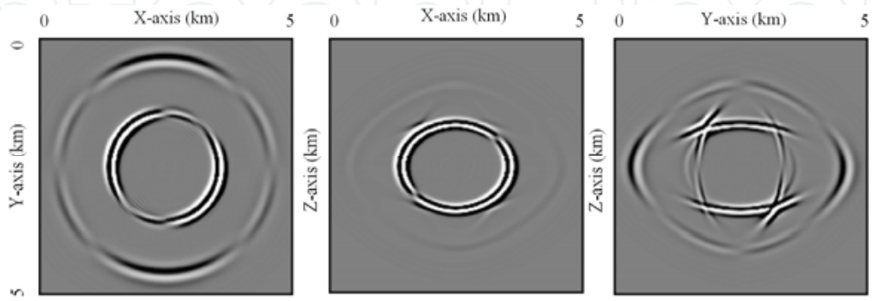

(a) (b) (c)

Fig. 21. Snapshots of elastic wave fields at time 0.7 sec for the y direction displacement (u_2) in the VTI medium, generated by the RK for (a) the xy plane, (b) the xz plane, and (c) the yz plane.

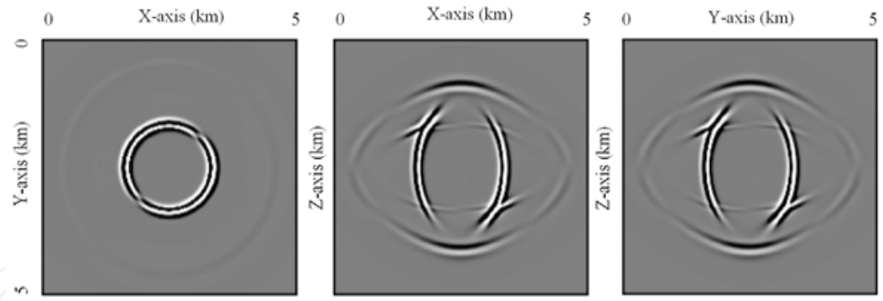

(a) (b) (c)

Fig. 22. Snapshots of elastic wave fields at time 0.7 sec for the z direction displacement (u_3) in the VTI medium, generated by the RK for (a) the *xy* plane, (b) the *xz* plane, and (c) the *yz* plane.

The wave field snapshots for u_1, u_2 and u_3 components at time 0.7 *sec* are shown in Figures 20, 21, and 22. Figure 20 shows the snapshots of the u_1 component in *xy*-, *xz*-, and *yz*-planes, whereas Figures 21 and 22 show the snapshots of u_2 and u_3 components in the three planes. The snapshots of the three displacement components in the *xy* plane (transverse plane), shown in Figures 20(a), 21(a), and 22(a), show that the wavefronts of *P* and *S* waves are a circle in the VTI medium, whereas other snapshots in Figures 20, 21, and 22 show that the wavefronts of *P* and *S* waves are an ellipse and the quasi-*P* (q*P*) and quasi-*SV* (q*SV*) waves show the directional dependence on propagation velocity. The *qSV* wavefronts have cusps and triplications depending on the value of c_{13} (Faria & Stoffa, 1994). Triplications can be observed in the horizontal component *qSV* wavefronts in the *xz* plane for the u_1 component (Fig. 20b), in the *yz*-plane for the u_2 component (Fig. 21c), and in the vertical component *qSV* wavefronts shown in Figures 22(b) and 22(c), respectively. Furthermore, in the VTI medium we can observe that the shear-wave splitting shows in Figures 20(b) and 21(c), and the arrival times of quasi-*SH* and *qSV* waves are different by comparing Figures 20(c) and 21(b) with Figures 20(b), 21(c), 22(b), and 22(c).

6. Summary

The two-stage RK method for solving 3D acoustic and elastic wave equations in isotropic and anisotropic media is developed via the four-stage fourth-order RK algorithm for solving ordinary differential equations and the high-degree multivariable interpolation approximation. In other words, the time derivatives are approximated via the two-stage fourth-order RK and the high-order space derivatives are calculated using the multivariable interpolation approximation. On the basis of such a structure, we have to first convert these high-order time derivatives to the spatial derivatives, which is similar to the high-order FD or so-called LWC methods (Lax and Wendroff, 1964; Dablain, 1986). However, the fourth-order RK method in approximating the high-order spatial derivatives is different from these high-order FD, LWC, and staggered-grid methods stated previously that only use the wave displacement at some grid points to approximate the high-order spatial derivatives or directly discretizing the original wave equation. This RK method uses simultaneously both the wave displacement and its gradients to approximate the high-order derivatives [see formulae (A3) to (A7)]. In other words, when determining these high-order spatial derivatives included in equation (8) or equation (9), the RK method uses not only the values

of the displacement U and the particle velocity W at the mesh point (i, j, k) and its neighboring gridpoints [see equations (A3)–(A7)], but also the values of the gradients of the displacement U and particle velocity W. Based on such a structure, the two-stage RK retains more wavefield information included in the displacement function, the particle velocity, and their gradients. As a result, the new RK can effectively suppress the numerical dispersion and source-generated noises caused by discretizing the wave equations when too-coarse grids are used or models have large velocity contrast between adjacent layers, and has higher spatial accuracy though the RK only uses a local difference operator that three gridpoints are used in a spatial direction.

Numerical dispersion analysis in section 4.1 and wave-field modeling results confirm our conclusion that the RK method has smaller numerical dispersion than the fourth-order LWC and SG methods. At the same time, these numerical results also imply that simultaneously using both the wave displacement, particle velocity, and their gradients to approximate the high-order derivatives is important for decreasing the numerical dispersion caused by the discretization of wave equations because the particle velocity and the gradients of both the wave displacement and the particle velocity include important wave-field information. On the other hand, using these connection relations such as equation (A2) and those omitted in this chapter between the grid point (i, j, k) and its neighboring nodes (i+p, j+q, k+r) (p, q, r=-1, 0, 1) keeps the continuity of gradients. The continuity and high accuracy (fourth-order accuracy in space) of gradients improve automatically the continuity of the stresses that are the linear combinations of gradients or the Hook sum, further resulting in the RK having less numerical dispersion when models have strong interfaces between adjacent layers. It suggests that we should consider the particle velocity and wave-gradient fields and the use of connection relations such as equation (A2), and so on, as we design a new numerical method to solve the 3D acoustic and elastic wave equations.

It appears that the CPU time of the two-stage RK is more than that of the fourth-order LWC and the SG methods, but in fact, because this method yields less numerical dispersion than both the LWC and SG methods, we can afford to increase the temporal increment through using coarser spatial increments to achieve the same accuracy as those of the LWC and the SG methods on a finer spatial grid with smaller time steps. Numerical computational results show that the RK method can also effectively suppress the numerical dispersion and the source-noise as the number of gridpoints in a minimum wavelength is about 3.3. Hence the total CPU time of the RK will not be larger than those of the LWC and the SG methods. As observed in our experiment, the computational speed of the RK is roughly 3.3 times of the fourth-order LWC and the SG on a fine grid to achieve the same accuracy as that of the RK, and the storage space required for the RK is only about 31.3% of the fourth-order LWC and about 27.8% of the fourth-order SG, respectively.

In conclusion, the 3D RK method has the following properties: (1) it can suppress effectively the numerical dispersion and source noise for practically coarse spatial and time steps; (2) it provides extra wave-field information including the particle velocity field and their time derivatives and spatial gradients, so the two-stage RK can be directly extended to solve the two-phase porous wave equations that include the first-order time derivatives such as Biot's porous wave equations (Biot 1956a,b); (3) it can increase greatly the computational efficiency and save storage space if larger spatial and temporal increments are used; (4) it only uses the local difference operator to obtain the high-order spatial accuracy. We initiate possible, more applications of the RK method in large-scale acoustic or seismic modeling, reverse time migration, and inversion based on the acoustic-wave equation, despite the computation time and memory requirements are the bottle-neck for their vast applications.

7. Appendices

7.1 Appendix A: evaluation of high-order derivatives

In order to numerically solve equation (8), we need to compute the high-order spatial derivatives $(\partial^{q+l+m}V / \partial x^q \partial y^l \partial z^m)^n_{i,j,k}$ $(2 \le q+l+m \le 3)$ so that the time advancing of the 3D RK equation (9) is implemented. To do this, following the local interpolation methods (Yang et al., 2007, 2010), we introduce the local interpolation function of spatial increments Δx , Δy , and Δz in the x, y, and z directions as follows:

$$G(\Delta x, \Delta y, \Delta z) = \sum_{r=0}^{5} \frac{1}{r!} (\Delta x \frac{\partial}{\partial x} + \Delta y \frac{\partial}{\partial y} + \Delta z \frac{\partial}{\partial z})^r V \,, \tag{A1}$$

which defines the interpolation relations between the grid point (i, j, k) and its 26 neighboring nodes such as (i, j, k+1), (i, j, k-1), (i, j+1, k+1), (i, j+1, k), (i, j+1, k-1), (i, j-1, k+1), (i, j-1, k), (i, j-1, k-1), (i+1, j, k+1), (i+1, j, k-1), (i+1, j+1, k+1), (i+1, j+1, k), (i+1, j+1, k-1), (i+1, j-1, k+1), (i+1, j-1, k), (i+1, j-1, k-1), (i+1, j, k), (i-1, j, k+1), (i-1, j, k-1), (i-1, j+1, k+1), (i-1, j+1, k), (i-1, j+1, k-1), (i-1, j-1, k+1), (i-1, j-1, k), (i-1, j-1, k-1), and (i-1, j, k). For example, at the grid point (i-1, j-1, k), we have the following interpolation relations:

$$\begin{aligned}
&\left[G(-\Delta x, -\Delta y, 0)\right]^n_{i,j,k} = V^n_{i-1,j-1,k}, \\
&\left[\frac{\partial}{\partial \Delta x} G(-\Delta x, -\Delta y, 0)\right]^n_{i,j,k} = \left(\frac{\partial}{\partial x} V\right)^n_{i-1,j-1,k}, \\
&\left[\frac{\partial}{\partial \Delta y} G(-\Delta x, -\Delta y, 0)\right]^n_{i,j,k} = \left(\frac{\partial}{\partial y} V\right)^n_{i-1,j-1,k}, \\
&\left[\frac{\partial}{\partial \Delta z} G(-\Delta x, -\Delta y, 0)\right]^n_{i,j,k} = \left(\frac{\partial}{\partial z} V\right)^n_{i-1,j-1,k}.
\end{aligned} \tag{A2}$$

Similarly, the rest 100 connection relations at other 25 neighboring nodes can be easily written.

From the 104 relations, we have similar approximation formulae as in the cited reference (Yang et al., 2010) to approximate the high-order spatial derivatives included in equation (8) or equation (9). For convenience, we list these approximation formulae used in the 3D RK method as follows

$$\left(\frac{\partial^2 V}{\partial g^2}\right)^n_{i,j,k} = \frac{2}{(\Delta g)^2} \delta_g^2 V^n_{i,j,k} - \frac{1}{2\Delta g}\left(E_g^1 - E_g^{-1}\right)\left(\frac{\partial V}{\partial g}\right)^n_{i,j,k}, \tag{A3}$$

$$\begin{aligned}
\left(\frac{\partial^2 V}{\partial g \partial e}\right)^n_{i,j,k} &= \frac{1}{2\Delta g}\left(E_g^1 - E_g^{-1}\right)\left(\frac{\partial V}{\partial e}\right)^n_{i,j,k} + \frac{1}{2\Delta e}\left(E_e^1 - E_e^{-1}\right)\left(\frac{\partial V}{\partial g}\right)^n_{i,j,k} \\
&\quad - \frac{1}{4\Delta g \Delta e}\left(E_g^1 E_e^1 + E_g^{-1} E_e^{-1} - E_g^1 E_e^{-1} - E_g^{-1} E_e^1\right) V^n_{i,j,k},
\end{aligned} \tag{A4}$$

$$\left(\frac{\partial^3 V}{\partial g^3}\right)_{i,j,k}^n = \frac{15}{2(\Delta g)^3}\left(E_g^1 - E_g^{-1}\right)V_{i,j,k}^n - \frac{3}{2(\Delta g)^2}\left(E_g^1 + 8I + E_g^{-1}\right)\left(\frac{\partial V}{\partial g}\right)_{i,j,k}^n, \tag{A5}$$

$$\begin{aligned}\left(\frac{\partial^3 V}{\partial g^2 \partial e}\right)_{i,j,k}^n &= \frac{1}{2\Delta g \Delta e}\left(-E_g^1 E_e^1 - E_g^{-1}E_e^{-1} + E_g^1 + E_g^{-1} - 2\delta_e^2\right)\left(\frac{\partial V}{\partial g}\right)_{i,j,k}^n \\ &+ \frac{1}{(\Delta g)^2}\delta_e^2\left(\frac{\partial V}{\partial e}\right)_{i,j,k}^n \\ &+ \frac{1}{4(\Delta g)^2 \Delta e}\left(5E_g^1 E_e^1 - 5E_g^{-1}E_e^{-1} + E_g^1 E_e^{-1} - E_g^{-1}E_e^1\right)V_{i,j,k}^n \\ &+ \frac{1}{4(\Delta g)^2 \Delta e}\left(-6E_g^1 + 6E_g^{-1} - 4E_e^1 + 4E_e^{-1}\right)V_{i,j,k}^n,\end{aligned} \tag{A6}$$

$$\begin{aligned}\left(\frac{\partial^3 V}{\partial x \partial y \partial z}\right)_{i,j,k}^n &= \frac{1}{4\Delta y \Delta z}\left(E_y^1 E_z^1 + E_y^{-1}E_z^{-1} - E_y^1 E_z^{-1} - E_y^{-1}E_z^1\right)\left(\frac{\partial V}{\partial x}\right)_{i,j,k}^n \\ &+ \frac{1}{4\Delta x \Delta z}\left(E_x^1 E_z^1 + E_x^{-1}E_z^{-1} - E_x^1 E_z^{-1} - E_x^{-1}E_z^1\right)\left(\frac{\partial V}{\partial y}\right)_{i,j,k}^n \\ &+ \frac{1}{4\Delta x \Delta y}\left(E_x^1 E_y^1 + E_x^{-1}E_y^{-1} - E_x^1 E_y^{-1} - E_x^{-1}E_y^1\right)\left(\frac{\partial V}{\partial z}\right)_{i,j,k}^n \\ &- \frac{1}{4\Delta x \Delta y \Delta z}\left(E_x^1 E_y^1 E_z^1 + E_x^{-1}E_y^{-1}E_z^{-1} + E_x^{-1}E_y^{-1}E_z^1 - E_x^1 E_y^1 E_z^{-1}\right)V_{i,j,k}^n \\ &- \frac{1}{4\Delta x \Delta y \Delta z}\left(E_x^{-1}E_y^1 E_z^{-1} - E_x^1 E_y^{-1}E_z^1 + E_x^1 E_y^{-1}E_z^{-1} - E_x^{-1}E_y^1 E_z^1\right)V_{i,j,k}^n.\end{aligned} \tag{A7}$$

where $g = x, y, z$ in formulae (A3) and (A5), and $g, e = x, y, z$ and $g \neq e$ in equations (A4) and (A6). $V_{i,j,k}^n$, $\left(\frac{\partial V}{\partial x}\right)_{i,j,k}^n$, $\left(\frac{\partial V}{\partial y}\right)_{i,j,k}^n$, $\left(\frac{\partial V}{\partial z}\right)_{i,j,k}^n$, and $\left(\frac{\partial^{q+l+m} V}{\partial x^q \partial y^l \partial z^m}\right)_{i,j,k}^n$ denote $V(i\Delta x, j\Delta y, k\Delta z, n\Delta t)$, $\frac{\partial}{\partial x}V(i\Delta x, j\Delta y, k\Delta z, n\Delta t)$, $\frac{\partial}{\partial y}V(i\Delta x, j\Delta y, k\Delta z, n\Delta t)$, $\frac{\partial}{\partial z}V(i\Delta x, j\Delta y, k\Delta z, n\Delta t)$, and $\frac{\partial^{q+l+m}}{\partial x^q \partial y^l \partial z^m}V(i\Delta x, j\Delta y, k\Delta z, n\Delta t)$, respectively. These notations δ_z^2 and E_z^1 in equations (A3) to (A7) are the second-order central difference operators and displacement operators in the z-direction, which are defined by

$$\delta_z^2 V_{i,j,k}^n = V_{i,j,k+1}^n - 2V_{i,j,k}^n + V_{i,j,k-1}^n,\ E_z^1 V_{i,j,k}^n = V_{i,j,k+1}^n, \text{ and } E_z^{-1}V_{i,j,k}^n = V_{i,j,k-1}^n.$$

Other operators such as δ_x^2, E_x^1, E_x^{-1} in the x-direction and δ_y^2, E_y^1, E_y^{-1} in the y-direction are defined similarly.

7.2 Appendix B: derivation of stability criteria

For the 3D homogeneous case, to obtain the stability condition of the two-stage RK method under the condition of $\Delta x = \Delta y = \Delta z = h$, we consider the 3D acoustic wave equation. Substituting the following solution

$$\overline{V}_{j,l,q}^{n} = \begin{pmatrix} V \\ \partial_x V \\ \partial_y V \\ \partial_z V \end{pmatrix}^{n} \exp\left[i(k_1 jh + k_2 lh + k_3 qh)\right] \tag{B1}$$

into the 3D RK method (9) together with relations (A3)-(A7), we can obtain the following equation

$$\overline{V}^{n+1} = G\overline{V}^{n}. \tag{B2}$$

In equation (B1), k_1, k_2 and k_3 are the components of the wave-number $k=(k_1, k_2, k_3)^{\mathrm{T}}$ and G is the growth matrix, whose detail expression is omitted because of its complex elements.

We assume that $\lambda_1, \lambda_2, \ldots$, and λ_p are the eigenvalues of G. We know that the scheme with the growth matrix G is stable only if $|\lambda_j| \le 1, j = 1,2,\cdots,p$ are satisfied. From which, we can obtain the stability criterion of the RK method for the 3D homogeneous case as follows

$$\alpha \le \alpha_{\max} \approx 0.577, \tag{B3}$$

where $\alpha_{\max}$ denotes the maximum value of the Courant number defined by $\alpha = c_0 \Delta t / \Delta x$, with the acoustic velocity being c_0.

Similarly, we can easily obtain the stability criteria (11) and (12) for the 1D and 2D cases.

7.3 Appendix C: derivation of the dispersion relation

To investigate and optimize the dispersion error, we derive the dispersion relation of the 3D RK method. For this, following the analysis methods presented in Dablain (1986) and Yang et al. (2006), we substitute the harmonic solution

$$\overline{V}_{j,l,q}^{n} = \overline{V}^{0} \cdot \exp(i(\omega n\tau) \cdot \exp\left[i(k_1 jh + k_2 lh + k_3 qh)\right] \tag{C1}$$

into the 3D RK equation (9), we can obtain the following linear equations about $\overline{V}^{0}$

$$\exp(i(\omega n\tau) \cdot \overline{V}^{0} = G \cdot \overline{V}^{0}, \tag{C2}$$

where $\overline{V}^{0} = (V^0, \partial_x V^0, \partial_y V^0, \partial_z V^0)^T$, ω is the angular frequency, and G is also the growth matrix. From (C2), we can obtain the following dispersion equation:

$$Det[\exp(i(\omega n\tau) \cdot I - G] = 0. \tag{C3}$$

Using the dispersion relation (C3), we obtain the ratio of the numerical velocity c_{num} to the phase velocity c_0 as follows

$$R = \frac{c_{num}}{c_0} = \frac{\omega\tau}{2\pi\alpha S_p} = \frac{\gamma}{2\pi\alpha S_p}, \tag{C4}$$

where α is the Courant number, $S_p = h/\lambda_{num} = h\omega/2\pi c_{num}$ is the spatial sampling ratio, and $\gamma = \omega\tau$ satisfies the dispersion equation (C3).

For comparison, here we also present the dispersion relation of the fourth-order staggered-grid (SG) scheme (Moczo et al., 2000). Using the definition of the spatial sampling ratio S_p and the Courant number α, we can obtain the following dispersion relation of the SG method through a series of derivation:

$$R = \frac{c_{num}}{c_0} = \frac{\omega\tau}{2\pi\alpha S_p} = \frac{\arcsin\left(\alpha\sqrt{x_1^2 + x_2^2 + x_3^2}\right)}{\pi\alpha S_p}, \tag{C5}$$

where

$$x_i = \frac{9}{8}\sin\theta_i - \frac{1}{24}\sin 3\theta_i,\ i = 1,2,3,$$

$$\theta_1 = \pi S_p \cos\varphi \sin\delta,$$

$$\theta_2 = \pi S_p \sin\varphi \sin\delta,$$

$$\theta_3 = \pi S_p \cos\delta,$$

in which $0 \le \delta < \pi$, and $0 \le \varphi < 2\pi$.

8. Acknowledgments

The authors acknowledge support provided by the National Science Fund for Distinguished Young Scholars of China (Grant No. 40725012). They also express their gratitude to other members of the Computational Geophysics Laboratory for their support.

9. References

Aki, K. & Richards, P. G. (1980). *Quantitative Seismology: Theory and Methods*, W.H. Freeman & Co., ISBN 0-935702-96-2, San Francisco, CA.

Biot, M. A. (1956a). Theory of propagation of elastic waves in a fluid-saturated porous solid, Ⅰ. Low-frequency range, *J. Acoust. Soc. Amer.*, Vol. 28, No. 2, pp. 168-178. ISSN 0001-4966

Biot, M. A. (1956b). Theory of propagation of elastic waves in a fluid-saturated porous solid, Ⅱ. Higher-frequency range. *J. Acoust. Soc. Amer.*, Vol. 28, No. 2, pp. 179-191. ISSN 0001-4966

Blanch, J. O. & Robertsson, J. O. A. (1997). A modified Lax-Wendroff correction for wave propagation in media described by Zener elements, *Geophys. J. Int.*, Vol. 131, No. 2, (November 1997), pp. 381-386, ISSN 0956-540X

Booth, D. C. & Crampin, S. (1983). The anisotropic reflectivity technique: anomalous arrives from an anisotropic upper mantle, *Geophys. J. R. astr. Soc.*, Vol. 72, No. 3, (March 1983), pp. 767-782, ISSN 0016-8009

Carcione, J. M. (1996). Wave propagation in anisotropic, saturated porous media: plane wave theory and numerical simulation, *J. Acoust. Soc. Amer.*, Vol. 99, No. 5, (May 1996), pp. 2655-2666, ISSN 0001-4966

Carcione, J. M. & Helle, H. B. (1999). Numerical solution of the poroviscoelastic wave equation on a staggered mesh, *J. Comput. Phys.*, Vol. 154, No. 2, (September 1999), pp. 520-527. ISSN 0021-9991

Carcione, J. M., S. Valle, S. & Lenzi, G. (1999). GPR modelling by the Fourier method: improvement of the algorithm, *Geophys. Prospect.*, Vol. 47, No. 6, pp. 1015-1029, ISSN 0016-8025

Chen, X. F. (1993). A systematic and efficient method of computing normal modes for multi-layered half-space, *Geophys. J. Int.*, Vol. 115, No. 2, (November 1993), pp. 391-409, ISSN 0956-540X

Dablain, M.A. (1986), The application of high-order differencing to the scalar wave equation: Geophysics, Vol. 51, No. 1, (January 1986), pp. 54-66, ISSN 0016-8033

de Hoop, A.T. (1960). A modification of Cagniard's method for solving seismic pulse problems, *Appl. Sci. Res.*, Vol. 8(B), No. 1, pp. 349–356, ISSN 0365-7140

Dimitri, K. & Jeroen, T. (2003). A perfectly matched layer absorbing boundary condition for the second-order seismic wave equation, *Geophys. J. Int.*, Vol. 154, No. 1, (June 2003), pp. 146–153, ISSN 0956-540X

Dumbser, M., Käser, M. & Toro, E. F. (2007). An arbitrary high-order Discontinuous Galerkin method for elastic waves on unstructured meshes – V. Local time stepping and p-adaptivity, *Geophys. J. Int.*, Vol. 171, No. 2, (November 2007), pp. 695-717, ISSN 0956-540X

Faria, E. L. & Stoffa P. L. (1994). Traveltime computation in transversely isotropic media, Geophysics, Vol. 59, No. 2, (February 1994), pp. 272-281, ISSN 0016-8033

Fei, T. & Larner, K. (1995). Elimination of numerical dispersion in finite difference modeling and migration by flux-corrected transport, *Geophysics*, Vol. 60, No. 6, (November-December 1995), pp. 1830–1842, ISSN 0016-8033

Fornberg, B. (1990). High-order finite differences and pseudo-spectral method on staggered grids, *SIAM J. Numer. Anal.*, Vol. 27, No. 4, (August 1990) pp. 904-918, ISSN 0036-1429

Holberg, O. (1987). Computational aspects of the choice of operator and sampling interval for numerical differentiation in large-scale simulation of wave phenomena, *Geophysical Prospecting*, Vol. 35, No. 6, (July 1987), pp. 629-655, ISSN 0016-8025

Igel, H., Mora, P. & Riollet, B. (1995). Anisotropic wave propagation through finite-difference grids, *Geophysics*, Vol. 60, No. 4, (July-August 1995), pp. 1203-1216, ISSN 0016-8033

Kelly, K., Ward, R., Treitel, S. & Alford, R. (1976). Synthetic seismograms: A finite-difference approach, *Geophysics*, Vol. 41, No. 1, (February 1976), pp. 2–27, ISSN 0016-8033

Kondoh, Y., Hosaka, Y. & Ishii, K. (1994). Kernel optimum nearly-analytical discretization algorithm applied to parabolic and hyperbolic equations, *Computers Math. Appl.*, Vol. 27(3), No. 3, (Feburay 1994), pp. 59–90, ISSN 0898-1221

Komatitsch, D. & Vilotte, J. P. (1998). The spectral element method: an efficient tool to simulate the seismic response of 2D and 3D geological structures, *Bull. Seism. Soc. Am.*, Vol. 88, No. 2, (April 1998), pp. 368-392, ISSN 0037-1106

Kosloff, D. & Baysal, E. (1982). Forward modeling by a Fourier method, *Geophysics*, Vol. 47, No. 10, (October 1982), pp. 1402-1412, ISSN 0016-8033

Lax, P. D. & Wendroff, B. (1964). Difference schemes for hyperbolic equations with high order of accuracy, *Commun. Pure Appl. Math. Vol.* 17, No. 3, (August 1964), pp. 381–398, ISSN

Mizutani, H., Geller, R. J. & Takeuchi, N. (2000). Comparison of accuracy and efficiency of time-domain schemes for calculating synthetic seismograms, *Phys. Earth Planet. Interiors*, Vol. 119, No. 1-2, (April 2000), pp. 75–97, ISSN 0031-9201

Moczo, P., Kristek, J. & Halada, L. (2000). 3D fourth-order staggered-grid finite-difference schemes: stability and grid dispersion, *Bull. Seism. Soc. Am.*, Vol. 90, No. 3, (June 2000), pp. 587-603, ISSN 0037-1106

Richtmyer, R. D. & Morton, K. W. (1967). Difference Methods for Initial Value Problems, *Interscience*, New York.

Sei, A. & Symes, W. (1995). Dispersion analysis of numerical wave propagation and its computational consequences, *J. Sci. Comput.*, Vol. 10, No. 1, (March 1995), pp. 1-27, ISSN 0885-7474

Vichnevetsky, R. (1979). Stability charts in the numerical approximation of partial differential equations: A review, *Mathematics and Computers in Simulation*, Vol. 21, , pp. 170–177, ISSN 0378-4754

Virieux, J. (1986). P-SV wave propagation in heterogeneous media: Velocity-stress finite-difference method, *Geophysics*, Vol. 51, No. 4, (April 1986), pp. 889-901, ISSN 0016-8033

Wang, S. Q., Yang, D. H. & Yang, K. D. (2002). Compact finite difference scheme for elastic equations, *J. Tsinghua Univ. (Sci. & Tech.)*, Vol. 42, No. 8, pp. 1128-1131. (in Chinese), ISSN 1000-0054

Yang, D. H., Liu, E., Zhang, Z. J. & Teng, J. W. 2002. Finite-difference modeling in two-dimensional anisotropic media using a flux-corrected transport technique, *Geophys. J. Int.*, Vol. 148, No. 2, (Feburary 2002), pp. 320-328, ISSN 0956-540X

Yang, D. H.,. Peng, J. M. Lu, M. & Terlaky, T. (2006). Optimal nearly analytic discrete approximation to the scalar wave equation, *Bull. Seism. Soc. Am.*, Vol. 96, No. 3 , (June 2006), pp. 1114-1130, ISSN 0037-1106

Yang, D. H., Song, G. J., Chen, S. & Hou, B. Y. (2007a). An improved nearly analytical discrete method: An efficient tool to simulate the seismic response of 2-D porous structures, *J. Geophys. Eng.*, Vol. 4, No. 1, (March 2007), pp. 40-52, ISSN 1742-2132

Yang D. H., Song, G. J. & Lu, M. (2007b). Optimally accurate nearly-analytic discrete scheme for wave-field simulation in 3D anisotropic media, *Bull. Seism. Soc. Am.*, Vol. 97, No. 5, (October 2007), pp. 1557-1569, ISSN 0037-1106

Yang, D. H., Teng, J. W., Zhang, Z. J. & Liu, E. (2003). A nearly-analytic discrete method for acoustic and elastic wave equations in anisotropic media, *Bull. Seism. Soc. Am.*, Vol. 93, No. 2, (April 2003), pp. 882–890, ISSN 0037-1106

Yang, D. H. & Wang, L. (2010). A split-step algorithm with effectively suppressing the numerical dispersion for 3D seismic propagation modeling, *Bull. Seism. Soc. Am.*, Vol. 100, No. 4, (August 2010), pp. 1470-1484, ISSN 0037-1106

Zhang, Z. J., Wang, G. J. & Harris, J. M. (1999). Multi-component wavefield simulation in viscous extensively dilatancy anisotropic media, *Phys. Earth planet Inter.*, Vol. 114, No. 1, (July 1999), pp. 25–38, ISSN 0031-9201

Zheng, H.S., Zhang, Z. J. & Liu, E. (2006). Non-linear seismic wave propagation in anisotropic media using the flux-corrected transport technique, *Geophys. J. Int.*, Vol. 165, No. 3, (June 2006), pp. 943-956, ISSN 0956-540X

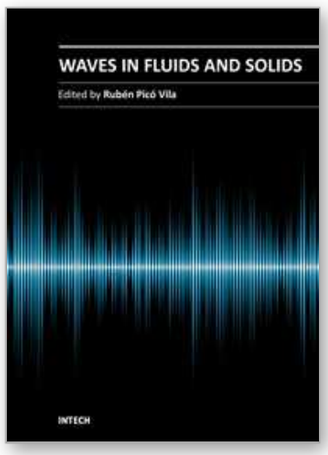

Waves in Fluids and Solids

Edited by Prof. Ruben Pico Vila

ISBN 978-953-307-285-2
Hard cover, 314 pages
Publisher InTech
Published online 22, September, 2011
Published in print edition September, 2011

Acoustics is an discipline that deals with many types of fields wave phenomena. Originally the field of Acoustics was consecrated to the sound, that is, the study of small pressure waves in air detected by the human ear. The scope of this field of physics has been extended to higher and lower frequencies and to higher intensity levels. Moreover, structural vibrations are also included in acoustics as a wave phenomena produced by elastic waves. This book is focused on acoustic waves in fluid media and elastic perturbations in heterogeneous media. Many different systems are analyzed in this book like layered media, solitons, piezoelectric substrates, crystalline systems, granular materials, interface waves, phononic crystals, acoustic levitation and soft media. Numerical methods are also presented as a fourth-order Runge-Kutta method and an inverse scattering method.

InTech Europe
University Campus STeP Ri
Slavka Krautzeka 83/A
51000 Rijeka, Croatia
Phone: +385 (51) 770 447
Fax: +385 (51) 686 166
www.intechopen.com

InTech China
Unit 405, Office Block, Hotel Equatorial Shanghai
No.65, Yan An Road (West), Shanghai, 200040, China
中国上海市延安西路65号上海国际贵都大饭店办公楼405单元
Phone: +86-21-62489820
Fax: +86-21-62489821

IntechOpen